

www.acsnano.org

## Elucidating the Origin of Plasmon-Generated Hot Holes in Water Oxidation

Jiawei Huang, Wenxiao Guo, Shuai He, Justin R. Mulcahy, Alvaro Montoya, Justin Goodsell, Namodhi Wijerathne, Alexander Angerhofer, and Wei David Wei\*

Cite This: https://doi.org/10.1021/acsnano.3c00758



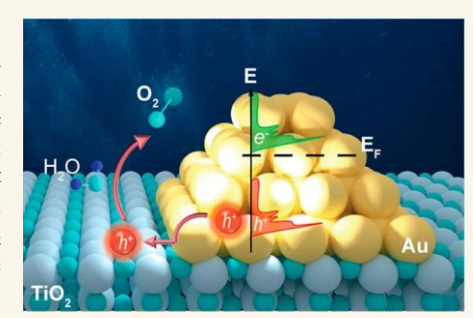
**ACCESS** 

Metrics & More

Article Recommendations

Supporting Information

ABSTRACT: Plasmon-generated hot electrons in metal/oxide heterostructures have been used extensively for driving photochemistry. However, little is known about the origin of plasmon-generated hot holes in promoting photochemical reactions. Herein, we discover that, during the nonradiative plasmon decay, the interband excitation rather than the intraband excitation generates energetic hot holes that enable to drive the water oxidation at the Au/TiO<sub>2</sub> interface. Distinct from lukewarm holes via the intraband excitation that only remain on Au, hot holes from the interband excitation are found to be transferred from Au into TiO<sub>2</sub> and stabilized by surface oxygen atoms on TiO<sub>2</sub>, making them available to oxidize adsorbed water molecules. Taken together, our studies provide spectroscopic evidence to clarify the photophysical process for exciting plasmon-generated hot



holes, unravel their atomic-level accumulation sites to maintain the strong oxidizing power in metal/oxide heterostructures, and aArm their crucial functions in governing photocatalytic oxidation reactions.

KEYWORDS: surface plasmon resonance, plasmon-generated hot holes, interband excitation, metal/oxide heterostructures, plasmon-driven photochemistry, in situ spectroscopy

he generation of hot carriers *via* localized surface plasmon resonance (LSPR) on metal nanoparticles (NPs) oRers a promising opportunity for driving photochemical reactions.<sup>1–12</sup> For instance, strategies have been developed to efficiently capture long-lived hot electrons within metal/oxide heterostructures for H<sub>2</sub> production,<sup>13–18</sup> CO<sub>2</sub> reduction,<sup>19–22</sup> and N<sub>2</sub> reduction reactions.<sup>23–25</sup> Despite the well-established understanding of hot-electron-driven processes,<sup>26–30</sup> to date, little is known about the other half of the hot-carrier equation: plasmon-generated hot holes (*i.e.*, the holes are thermodynamically available to participate in chemical reactions, such as water oxidation reaction, rather than relaxing to the Au Fermi level under steady-state conditions) in photocatalysis. Although recent studies have observed that plasmon-generated hot holes at the metal/oxide interface were capable of driving the water oxidation

reaction,<sup>31</sup> most eRorts were focused on optimizing the reaction activity,<sup>32–42</sup> and a clear identification of the origin of those hot holes in the water oxidation has not been fully explored.

In this contribution, we employed *in situ* electron paramagnetic resonance (EPR) spectroscopy to follow the fate of plasmon-generated hot holes at the Au/TiO<sub>2</sub> interface to elucidate their origin in oxidation reactions. Our studies revealed that the plasmon-assisted interband excitation (d-band to sp-band transitions with holes in the d band of Au)

rather than the plasmon-assisted intraband excitation (sp-band to sp-band transitions with holes in the sp band of Au) generated energetic hot holes that promoted the water oxidation at the Au/TiO2 interface. Compared to lukewarm sp-band holes that only stayed on Au NPs, hot d-band holes were transferred from Au NPs to interfacial oxygen atoms on the TiO2 surface. The localization of plasmon-generated hot holes on surface oxygen atoms of TiO2 suppressed the fast hole relaxation to the Au Fermi level and therefore maintained their energy near the valence band maximum of TiO2 under steadystate conditions. Our spectroscopic studies further demonstrated that those hot holes were transferred from the TiO2 surface into oxygen atoms of adsorbed water molecules, highlighting the importance of the plasmon-assisted interband excitation in facilitating the water oxidation at the metal/oxide interface.

Received: January 25, 2023 Accepted: April 7, 2023



#### **RESULTS AND DISCUSSION**

Identification of Atomic-Level Accumulation Sites of Hot Holes at Au/TiO2 Interface in Water Oxidation. Au NPs with an average diameter of 4.3  $\pm$  0.6 nm were grown on commercially available P25 (Degussa) via a deposition-precipitation method (Figure S1A).<sup>43</sup> A LSPR feature arising from Au NPs was found at approximately 556 nm ( $\lambda_{\rm LSPR}$ ) for Au/TiO2 heterostructures (Figure S1C), while TiO2 itself only absorbed light in the ultraviolet (UV) region (Figure S1D). These distinct optical properties of Au NPs and TiO2 provided an opportunity to solely excite plasmon-generated hot carriers in Au/TiO2 heterostructures using visible-light irradiation. High-resolution transmission electron microscopy (HRTEM) confirmed that a heterogeneous interface was constructed between Au and TiO2 (Figure S1B), creating a pathway for the plasmon-mediated interfacial carrier transfer.<sup>44</sup>

Au/SiO<sub>2</sub> was also prepared using the same depositionprecipitation method. Since SiO<sub>2</sub> is an insulating support, 45 the plasmon-generated hot holes on Au NPs should quickly relax to the Au Fermi level (approximately -5.1 eV vs vacuum in the sp band)46 due to the continuous band structure of Au and electron-electron and electron-phonon interactions in Au.<sup>47</sup> As a result, those lukewarm holes on Au should be thermodynamically unfavorable to drive the water oxidation reaction (approximately -5.73 eV vs vacuum).<sup>48,49</sup> Indeed, Au/SiO<sub>2</sub> heterostructures were inactive for the water oxidation under visible-light irradiation ( $\lambda > 495$  nm) (Figure S2A and see the Supporting Information for further discussions). However, Au/TiO<sub>2</sub> heterostructures exhibited a photocatalytic activity for water oxidation under visible-light irradiation ( $\lambda > 495$  nm) (Figure S2A), suggesting the interfacial transfer of hot holes from Au into TiO2 during the water oxidation reaction. The plasmon-mediated interfacial hot-hole transfer from Au into

electrons at the Ti centers of  $TiO_2$  produced EPR-active  $Ti^{3+}$  species. The EPR feature of  $Ti^{3+}$  in the rutile  $TiO_2$  was shown at the g values of ca. 1.976 and 1.953 (*i.e.*, denoted as the green dashed lines in our EPR spectra), while the g values of  $Ti^{3+}$  species in the anatase  $TiO_2$  were found at ca. 1.990 and 1.961

TiO<sub>2</sub> was further verified using *in situ* EPR spectroscopy.

Previous studies have reported that the accumulation of

(i.e., denoted as light-purple dashed lines in our EPR spectra).50-52 Meanwhile, the localization of holes at oxygen atoms of TiO2 also created EPR-active O- species with the g values of ca. 2.003, 2.015, and 2.024 (denoted as  $h^+(O^-)$  and black dashed lines in our EPR spectra).53-56 As shown in Figure 1A and Figures S4 and S5, under visible-light irradiation  $(\lambda > 495 \text{ nm})$ , plasmon-generated hot electrons were transferred from Au NPs into TiO2 and increased the Ti3+ signal intensity. Meanwhile, a new EPR feature appeared at the position (q = 2.003, 2.015, and 2.024 in Figure 1A and FigureS5) that is consistent with the characteristic of photogenerated holes on surface oxygen atoms of TiO2 (i.e., in the form of Ti4+O2-Ti4+O• -).53-56 Since bare TiO2 does not absorb visible light (Figure S1D), those holes on surface oxygen atoms of TiO<sub>2</sub> (denoted as  $h^+(O^-)$ ) must originate from the plasmongenerated hot holes on Au that were transferred into TiO2 and then remained on surface oxygen atoms under steady-state conditions (Figure 1B). Indeed, no  $h^+$  (O<sup>-</sup>) signal was observable on bare TiO<sub>2</sub> under visible-light irradiation (λ > 495 nm) (Figure S6), clearly demonstrating that the

> 495 nm) (Figure S6), clearly demonstrating that the irradiation wavelength longer than 495 nm is unable to generate holes from TiO<sub>2</sub> excitation.

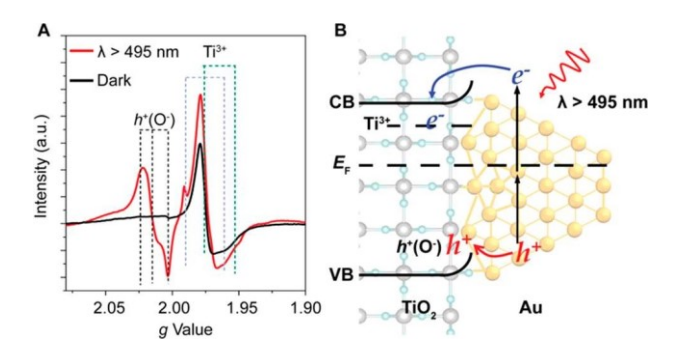


Figure 1. Accumulation sites of hot holes in  $Au/TiO_2$  heterostructures. (A) In situ EPR spectra of  $Au/TiO_2$  heterostructures in the dark (black) and under visible-light irradiation ( $\lambda > 495$  nm) (red) at 5 K under He condition. (B) Schematic of accumulation sites where hot carriers reside within  $Au/TiO_2$  heterostructures, showing the interfacial hot-hole transfer from Au NPs to surface oxygen atoms of  $TiO_2$  and the interfacial hot-electron transfer from Au NPs to  $Ti^{3+}$  of  $TiO_2$ , respectively. The

cyan, gray, and yellow dots stand for oxygen, titanium, and gold atoms, respectively. CB and VB are the conduction band and the valence band of TiO. E is the Fermi level of Au/TiO

heterostructures.

It should be noted that plasmon-generated hot electrons

injected into the conduction band of TiO<sub>2</sub> were swept away from the interface by the built-in electric field located in the depletion layer,<sup>29</sup> efficiently preventing the recombination between those hot electrons and hot holes on surface oxygen atoms of interfacial TiO<sub>2</sub>. It is also known that the valence band of TiO<sub>2</sub> is mainly composed of O<sub>2p</sub>, suggesting that the energy level of those hot holes on surface oxygen atoms of TiO<sub>2</sub> are located near the valence band maximum (approximately –7.4 eV vs vacuum). 48,49 Therefore, the localization of plasmon-generated hot holes at interfacial TiO<sub>2</sub> makes them thermodynamically favorable to drive the water oxidation reaction (approximately –5.73 eV vs vacuum) at the Au/TiO interface.

### Further Insights into Hot-Hole Distribution at Au/TiO<sub>2</sub>Interface for Water Oxidation. Previous studies

reported that the  $O_2$  species also exhibited similar g values (g=2.003, 2.010, and 2.026) as the EPR feature of  $h^+(O^-).^{53}$  In order to exclude the possibility that the visible-light-induced new EPR feature in Figure 1A was originated from the hotelectron-generated  $O_2^-$  species, we further created oxygen vacancies on the  $TiO_2$  surface in Au/ $TiO_2$  heterostructures by utilizing the photodeposition method (see the Supporting Information for further discussions about the formation of oxygen vacancies). It is noted that the presence of oxygen vacancies on the  $TiO_2$  surface not only enables the generation of  $O_2^-$  species by functioning as trapping centers for hot electrons and adsorption sites of  $O_2$  molecules  $O_2^-$  but also reduces the number of plasmon-generated hot holes on  $O_2^-$  by acting as hot electron—hole recombination centers.

For Au/TiO<sub>2</sub> heterostructures prepared by the photodeposition method, the EPR feature (g = 2.003) of electrons trapped at oxygen vacancies of TiO<sub>2</sub> (denoted as  $e^-$  (V<sub>o</sub>)) was observable in the dark (Figure 2A and Figure S7),<sup>60,61</sup> showing that oxygen vacancies were created on TiO<sub>2</sub>. Because the energy level of oxygen vacancies is approximately 1.18 eV below the conduction band edge of TiO<sub>2</sub> (i.e., the energy of Ti<sup>3+</sup>),<sup>57</sup> the formation of low-energy oxygen vacancy states traps the majority of electrons in TiO<sub>2</sub> and results in a much

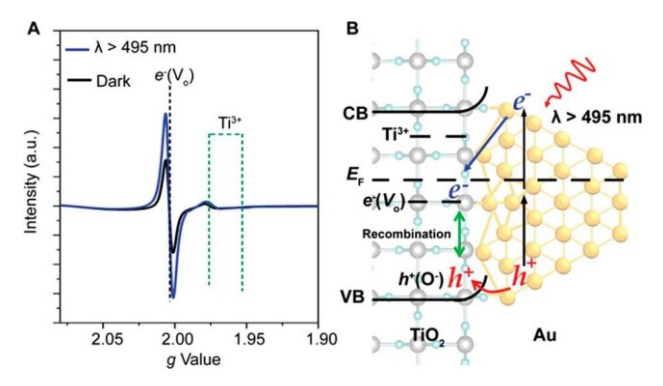


Figure 2. Accumulation sites of hot holes in  $Au/TiO_2$  heterostructures with oxygen vacancies. (A) In situ EPR spectra of  $Au/TiO_2$  heterostructures with surface oxygen vacancies in the dark (black) and under visible-light irradiation ( $\lambda > 495$  nm) (blue) at 5 K under He condition. (B) Schematic of accumulation sites where hot carriers reside within  $Au/TiO_2$  heterostructures, showing the interfacial hot-electron transfer from Au NPs to surface oxygen vacancies of  $TiO_2$  to further recombine with plasmon-generated hot holes on interfacial oxygen atoms of  $TiO_2$ .

higher relative intensity of  $e^-$  (V<sub>o</sub>) than Ti<sup>3+</sup> signal (Figure 2A, black curve). Under the visible-light irradiation ( $\lambda > 495$  nm), only the enhancement of  $e^-$  (V<sub>o</sub>) was detected (Figure 2A), while the EPR feature (g=2.003, 2.015, and 2.024) completely disappeared. This result clearly showed that the visible-light-induced EPR feature at the g values of 2.003, 2.015, and 2.024 in Figure 1A was not originated from O<sub>2</sub><sup>-</sup> species, whose EPR signal intensity should be greatly enhanced by the formation of surface oxygen vacancies on TiO<sub>2</sub>. As shown in Figure 2B, in Au/TiO<sub>2</sub> heterostructures with oxygen vacancies, plasmongenerated hot electrons were directly transferred to lower-energy surface oxygen vacancies. This hot-electron transfer pathway was confirmed by an enhancement of  $e^-$  (V) feature

and almost no increase of Ti3+ intensity under visible-light irradiation in the presence of oxygen vacancies (the blue curve in Figure 2A). Those hot electrons at surface oxygen vacancies of TiO2 further recombined with hot holes that were localized at interfacial oxygen atoms on the TiO<sub>2</sub> surface (Figure 2B). As a result, hot holes only remained in Au NPs (i.e., EPR silent) and no EPR feature of  $h^+(O^-)$  from  $TiO_2$  was observable for Au/TiO<sub>2</sub> heterostructures with oxygen vacancies under steadystate conditions. It should be noted that the photodeposition method creates oxygen vacancies on both the TiO2 surface and Au/TiO2 interface (i.e., perimeter area of Au/TiO2 interface) followed by the surface photocorrosion mechanism. Upon plasmon excitation, hot electrons from Au are trapped by oxygen vacancies on both the TiO2 surface and the Au/TiO2 interface. However, only the hot electrons at interfacial oxygen vacancies are able to recombine with interband hot holes at the interfacial TiO<sub>2</sub>.

Recent studies have found that the formation of oxygen vacancies on Au/TiO<sub>2</sub> significantly suppressed the activity of plasmon-driven water oxidation.<sup>59</sup> This observation together with our EPR studies into the spatial distribution of hot holes in Au/TiO<sub>2</sub> heterostructures with oxygen vacancies further confirms that hot holes that stay in Au NPs in the presence of oxygen vacancies are not energetic enough to drive water oxidation. Instead, hot holes have to transfer from Au into TiO<sub>2</sub> and maintain their strong oxidizing power at interfacial oxygen atoms on TiO<sub>2</sub> to oxidize adsorbed water molecules.

Origin of Plasmon-Generated Hot Holes at Au/TiO2 Interface. Upon plasmon excitation, the damping from the plasmon resonance oRers additional pathways (i.e., interband excitation from d-band to sp-band, and intraband excitation from sp-band to sp-band) for the electronic transitions. 62,63 It has been reported that the generation of sp-band holes via intraband excitation follows the LSPR feature and reaches the maximum at λ<sub>LSPR</sub>.64,65 The energy of those intraband hot holes exhibits a nearly uniform distribution from the Fermi level up to the photon energy. On the other hand, the interband excitation only occurs when the energy from the damping of plasmon resonance is larger than the interband threshold energy ( $E_{int} = ca. 1.6-1.8 \text{ eV}$  for plasmonic Al, Au, and Cu;  $E_{int} = ca. 3.5 \text{ eV for Ag}, \frac{62,66,67}{9}$  generating hot holes at the d-band far below the Fermi level. Rather than following the LSPR feature, the yield of interband hot holes continuously increases when irradiating with a shorter wavelength than  $\lambda_{\text{LSPR}}$ ,  $^{62,64,65}$  As shown in Figure 3A and Figure S8, the EPR

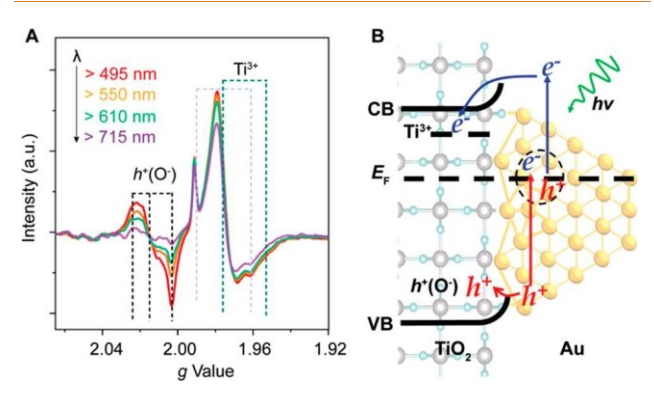


Figure 3. Identification of the origin of hot holes on surface oxygen atoms of TiO<sub>2</sub> through wavelength-dependent EPR measurements. (A) In situ EPR spectra of Au/TiO<sub>2</sub> heterostructures under diRerent irradiation wavelengths at 5 K under He conditions. The diRerent wavelength-dependent EPR intensities of h<sup>+</sup>(O<sup>-</sup>) and Ti<sup>3+</sup> features exclude the impact of minor intensity variation between each irradiation wavelength on assigning the excitation mechanism of hot holes and hot electrons. (B) Schematic of the origin of hot holes accumulated on interfacial oxygen atoms of TiO<sub>2</sub>.

intensities of Ti<sup>3+</sup> species (*i.e.*, hot electrons at Ti centers of TiO<sub>2</sub>) almost kept the same when irradiating with wavelengths containing  $\lambda_{\rm LSPR}$  (*i.e.*,  $\lambda > 495$  and 550 nm) but decreased once using longer wavelengths than  $\lambda_{\rm LSPR}$  (*i.e.*,  $\lambda > 610$  and 715 nm). This observation clearly showed that hot electrons trapped at Ti<sup>3+</sup> species of TiO<sub>2</sub> were generated *via* the plasmon-assisted intraband excitation of Au NPs. Meanwhile, the EPR intensity of  $h^+(\text{O}^-)$  continuously increased when varying the irradiation wavelength from 715 to 495 nm (Figure 3A and Figure S8), strongly suggesting that hot holes accumulated on surface oxygen atoms of TiO<sub>2</sub> were generated from plasmon-assisted interband excitations.

Moreover, both intraband and interband excitations take place when hv is larger than 1.8 eV ( $E_{\rm int}$  of Au), whereas only the intraband excitation is allowed when hv is less than 1.8 eV. Indeed, we found that, when irradiating with  $\lambda > 780$  nm (hv < 1.6 eV), the increase of the EPR feature of  $Ti^{3+}$  species (due to the transfer of electrons from Au into  $TiO_2$ ) was still observable but the EPR feature of  $h^+$  (O<sup>-</sup>) completely disappeared (Figure 4A), clearly showing that lukewarm spband holes from the intraband excitation were not energetic

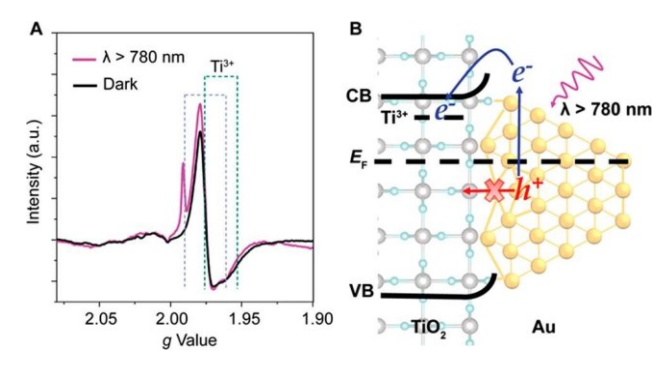


Figure 4. Identification of the origin of hot holes on surface oxygen atoms of  ${\rm TiO_2}$  by only exciting intraband transitions. (A) In situ EPR spectra of  ${\rm Au/TiO_2}$  heterostructures in the dark (black) and under the light irradiation ( $\lambda > 780$  nm) (pink) at 5 K under He conditions. (B) Schematic of the spatial distribution of hot electrons and lukewarm holes generated by the intraband excitation in  ${\rm Au/TiO_2}$  heterostructures.

enough to be transferred from Au into TiO<sub>2</sub> (Figure 4B). Taken together, we attributed the origin of hot holes residing on surface oxygen atoms of TiO<sub>2</sub> at the Au/TiO<sub>2</sub> interface to the synergetic eRect between plasmon-assisted intraband and interband excitations: lukewarm sp-band holes from the plasmon-assisted intraband excitation recombined with electrons generated by the plasmon-assisted interband excitation, resulting in long-lived and hot d-band holes that were capable of transferring from Au to interfacial oxygen atoms on the TiO<sub>2</sub> surface (Figure 3B).<sup>68</sup>

Interfacial Transfer of Interband Hot Holes in Water Oxidation. The transfer of hot d-band holes from the  $TiO_2$  surface to adsorbed water molecules in the process of water oxidation reaction was further affirmed using EPR spectroscopy. As shown in Figure 5A and Figure S9, the EPR feature of  $h^+(O^-)$  was significantly enhanced in the presence of water molecules as compared to dried  $Au/TiO_2$  heterostructures. However, there was no  $h^+(O^-)$  observed on  $Au/SiO_2$  heterostructures in the presence of water molecules (Figure S10). This significant comparison confirmed that lukewarm spband holes remaining on Au NPs in  $Au/SiO_2$  heterostructures

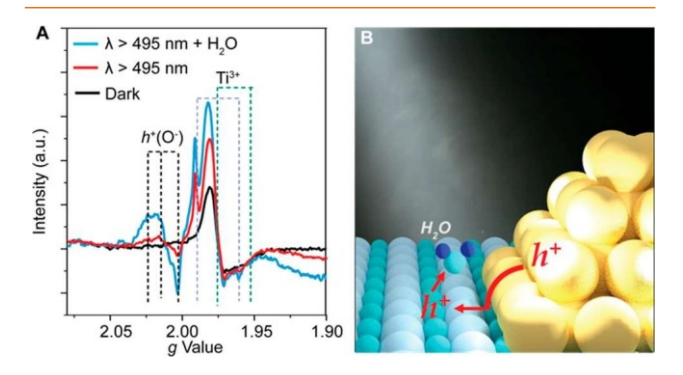


Figure 5. Plasmon-driven water oxidation on Au/TiO<sub>2</sub> heterostructures by using hot d-band holes on surface oxygen atoms of TiO<sub>2</sub>. (A) EPR spectra of Au/TiO<sub>2</sub> heterostructures in the dark (black), under visible-light irradiation ( $\lambda > 495$  nm) (red), and under visible-light irradiation in the presence of water molecules (blue). These EPR measurements were conducted at 90 K. (B) Scheme of hot-hole transfer from the TiO<sub>2</sub> surface to oxygen atoms of adsorbed water molecules, increasing the amount of h<sup>+</sup>(O<sup>-</sup>) species.

were unable to transfer to water molecules to promote the water oxidation reaction. In contrast, under steady-state conditions (with continuous light irradiation), the transfer of plasmon-generated interband hot holes from Au to TiO2 reached an equilibrium. The addition of water resulted in a shift of the equilibrium due to the transfer of hot holes from TiO2 to adsorbed water molecules, allowing the transfer of additional interband hot holes from Au to TiO2. It is noted that  $O^-$  species in water also contribute to the EPR signal of  $h^+$ (O-) (see the SI for detailed chemical descriptions about how the  $O^-$  species is formed from water), since g values of waterderived oxygen radicals were reported at around 2.007, 2.019, and 2.027, similar to g values of  $h^+$  (O<sup>-</sup>) in dried Au/TiO<sub>2</sub>.69 Therefore, the addition of water to Au/TiO<sub>2</sub> produced more O- species as compared to the number of O- species only originating from TiO2 in dried samples, resulting in the increase of the EPR signal for  $h^+$  (O<sup>-</sup>) in the presence of water. This water-assisted h+(O-) enhancement for Au/TiO2 heterostructures supported that hot holes on the surface oxygen atoms of TiO<sub>2</sub> indeed participated in the water oxidation reaction (Figure 5B).

#### **CONCLUSION**

In summary, we successfully clarified the origin of plasmongenerated hot holes in promoting the water oxidation reaction at the Au/TiO2 interface. Hot holes that determined the activity of water oxidation were derived from the plasmonassisted interband excitation of Au NPs. Our studies showed that distinct from lukewarm sp-band holes via the plasmonassisted intraband excitation that only remained on Au NPs, energetic d-band holes from the plasmon-assisted interband excitation were transferred from Au NPs into TiO2 where surface oxygen atoms stabilized those hot holes and maintained their energy over extended time scales, making them thermodynamically favorable to participate in the water oxidation reaction. It is reported that the action spectrum of hot-hole-driven alcohol oxidation and water oxidation also exhibited a higher reaction rate under the shorter irradiation wavelength.70-72 The consistency between the wavelengthdependent intensity variation of h<sup>+</sup> (O<sup>-</sup>) feature (Figure 3A) and the reported action spectra of plasmon-driven photochemistry provides a unified picture, where the interband hot holes are more energetic than intraband holes for redox reactions in aqueous media. 70-74 More importantly, our in situ spectroscopic studies further identify atomic-level accumulation sites of interband hot holes at the metal/oxide interface, unraveling how interband hot holes maintain their strong oxidizing power for photochemistry over a time scale ranging from milliseconds to seconds. We also found that the manipulation of interfacial atomic structures (with or without oxygen vacancies) enables to significantly alter the atomic distribution of hot holes in metal/oxide heterostructures. Taken together, our results establish a comprehensive description of the underlying photophysical process of exciting and harvesting energetic hot holes in plasmon-driven chemical reactions on metal/oxide heterostructures and thus provide guidance for the development of advanced plasmonic photocatalysts for efficient hot-hole-driven oxidation reactions.

#### **METHODS**

Synthesis of Au/TiO $_2$  Heterostructures. Au/TiO $_2$  heterostructures were prepared by a deposition-precipitation method to grow approximately 4–5 nm Au NPs onto commercially available P25

(Degussa) supports.<sup>15</sup> In detail, 1.1 g of P25 was dispersed into 100 mL of nanopure H<sub>2</sub>O under continuous sonication in a 250 mL round-bottom flask. The mixture was placed in an oil bath and stirred at 333 K for 30 min. A 25 mM HAuCl<sub>4</sub> solution (2.2 mL) was then added to achieve the desired 1 wt % Au loading. NH<sub>4</sub>OH (10%) was dropped to adjust the pH to 9-10, and the mixture was further stirred in the oil bath at 333 K for another 4 h. The solid was collected via centrifugation at 10,000 rpm for 10 min and then washed with nanopure H2O. The washing process was repeated three times, followed by drying the sample at 333 K overnight in the oven. The powder sample was finally annealed at 483 K for 3 h in the oven to create Au/TiO2 heterostructures. The deposition-precipitation method was also utilized to deposit Au NPs onto SiO2 supports to construct Au/SiO<sub>2</sub> heterostructures. For 1 wt % Au/TiO<sub>2</sub> heterostructures prepared by a photodeposition method, 50 mg of P25 and 0.1 mL of a 25 mM HAuCl<sub>4</sub> were dispersed in a 100 mL aqueous solution of 2% methanol in a flask, with subsequent irradiation under a 500 W Hg lamp (Newport, Inc.) equipped with a 280-420 nm filter (Newport, Inc. and  $I_0 = 250 \text{ mW/cm}^2$ ) in the atmosphere with stirring for 0.5 h. The solid was collected via centrifugation at 10,000 rpm for 10 min and then washed with nanopure H2O. The washing process was repeated three times, followed by drying the sample at 333 K overnight in the oven.

Electron Paramagnetic Resonance Spectroscopy Data Collection and Analysis. EPR experiments were performed on a Bruker ELEXSYS-II E500 CW X-band spectrometer within a super high-Q cavity (ER 4123SHQE), equipped with an ESR900 Oxford Instruments helium flow cryostat for low-temperature experiments. For EPR experiments conducted at 5 K,  $40 \pm 2$  mg of a sample was loaded into a quartz EPR tube (approximately 4 mm inner diameter), sealed in the He conditions, and placed within the microwave cavity. For the EPR study of hot-hole-driven water oxidation, the temperature was elevated to 90 K in order to facilitate the transfer of hot holes from Au/TiO2 heterostructures into water molecules. 55 In detail, 36 µL of water was added into the EPR tube and mixed with 40 ± 2 mg of the sample. After that, the EPR tube was capped and placed within the microwave cavity. Since the EPR study of hot-holedriven water oxidation was conducted under the air conditions, it was necessary to study whether the hot-electron-generated O2- species also created an EPR feature, which exhibited similar g values as the EPR feature of  $h^+(O^-)$ . Compared to the EPR spectrum collected under the air condition, almost no variation in the intensity of  $h^+(O^-)$ was observable after purging Ar gas into the EPR tube (Figure S11), excluding the existence of O<sub>2</sub><sup>-</sup> species in the EPR spectrum. All EPR spectra were collected using the following instrument parameters: 100 kHz modulation frequency, 3 G modulation amplitude, 40 ms conversion time, 15 mW microwave power, and 60 dB receiver gain. A total of 20 scans were used to acquire a signal average for each sample. Optical excitation of the sample was performed directly within the microwave cavity using a 300 W Xe lamp (Newport, Inc.) equipped with optical long-pass filters (Thor Laboratories, Inc.) to irradiate the sample through the optical port of resonator. For the optical excitation using optical long-pass filters (Thor Laboratories, Inc.), samples were irradiated within the microwave cavity under an incident light intensity of  $400 \pm 50 \text{ mW cm}^{-2}$  for 60 min prior to datacollection. The background signal measured from the pure quartz EPR tube was removed from EPR spectra, and the q values used in the EPR simulation are summarized in Table S1. Simulated EPR spectra were generated using the EasySpin toolbox in MATLAB.75

Photocatalytic Reaction Test. The water oxidation reaction was carried out in a closed gas circulation and evacuation system. Au/  $TiO_2$  and  $Au/SiO_2$  heterostructures were used as photocatalysts. Fifty milligrams of photocatalysts were dispersed into a 100 mL of 5 mM  $Fe(NO_3)_3$  aqueous solution with magnetic stirring. After that, the system was degassed, followed by purging Ar into the system. Optical excitations of the sample were performed using a 300 W Xe lamp (Newport, Inc.) equipped with a 495 nm long-pass filter (Thor Laboratories, Inc.). In all optical experiments, the sample was irradiated under an incident light power of 300  $\pm$  50 mW cm<sup>-2</sup>. The gas system was circulated for 5 min in every 30 min. The

generation of  $\rm O_2$  molecules was detected using a gas chromatograph (Shimadzu GC-2014) equipped with a 60/80 Mol Sieve 5A column and a thermal conductivity detector (TCD) maintained at 35 °C with Ar as the carrier gas.

Other Characterizations. High-resolution transmission electron microscopy (HRTEM) and transmission electron microscopy (TEM) were conducted on a JEOL 2010F HRTEM operated at 200 kV, located at MAIC at the University of Florida (UF). DiRuse reflectance measurements of photocatalysts were collected on a Shimadzu UV-2600 spectrophotometer equipped with the diRuse reflectance integrating sphere accessory (ISR-2600Plus).

#### **ASSOCIATED CONTENT**

#### ★ Supporting Information

The Supporting Information is available free of charge at https://pubs.acs.org/doi/10.1021/acsnano.3c00758.

Discussions of materials used, plasmon-driven water oxidation on Au/TiO<sub>2</sub> and Au/SiO<sub>2</sub> heterostructures, formation of oxygen vacancies on TiO<sub>2</sub> using photo-deposition method, and chemical descriptions about the formation of O<sup>-</sup> species from water, figures of TEM and UV-vis of Au/TiO<sub>2</sub> heterostructures, additional data of

water oxidation on Au/TiO<sub>2</sub> and TiO<sub>2</sub> under visiblelight irradiations, TEM characterization of Au/TiO<sub>2</sub> heterostructures after the plasmon-driven water oxidation reaction, experimental and simulated X-band EPR spectra of Au/TiO<sub>2</sub> heterostructures, *in situ* EPR spectra of Au/TiO<sub>2</sub> heterostructures and bare TiO<sub>2</sub>, and threedimensional X-band EPR spectra of Au/TiO<sub>2</sub> heterostructures under diRerent irradiation wavelengths, and table of summary of *g* values used for simulation of Xband EPR spectra (PDF)

#### **AUTHOR INFORMATION**

#### **Corresponding Author**

Wei David Wei – Department of Chemistry and Center for Catalysis, University of Florida, Gainesville, Florida 32611, United States; orcid.org/0000-0002-3121-5798; Email: wei@chem.ufl.edu

#### Authors

Jiawei Huang – Department of Chemistry and Center for Catalysis, University of Florida, Gainesville, Florida 32611, United States; Present Address: Department of Chemistry and Biochemistry and the Oregon Center for Electrochemistry, University of Oregon, Eugene, Oregon 97403, United States; orcid.org/0000-0002-5184-2510

Wenxiao Guo – Department of Chemistry and Center for Catalysis, University of Florida, Gainesville, Florida 32611, United States; Present Address: Department of Chemical and Biological Engineering, University of Wisconsin – Madison, Madison, Wisconsin 53706, United States.;

orcid.org/0000-0002-6674-9714

Shuai He – Department of Chemistry and Center for Catalysis, University of Florida, Gainesville, Florida 32611, United States

Justin R. Mulcahy – Department of Chemistry and Center for Catalysis, University of Florida, Gainesville, Florida 32611, United States; Orcid.org/0000-0001-5975-2854

Alvaro Montoya – Department of Chemistry and Center for Catalysis, University of Florida, Gainesville, Florida 32611, United States

- Justin Goodsell Department of Chemistry and Center for Catalysis, University of Florida, Gainesville, Florida 32611, United States
- Namodhi Wijerathne Department of Chemistry and Center for Catalysis, University of Florida, Gainesville, Florida 32611, United States
- Alexander Angerhofer Department of Chemistry and Center for Catalysis, University of Florida, Gainesville, Florida 32611, United States; orcid.org/0000-0002-8580-6024

Complete contact information is available at: https://pubs.acs.org/10.1021/acsnano.3c00758

#### Notes

The authors declare no competing financial interest.

#### **ACKNOWLEDGMENTS**

This work was supported by the National Science Foundation under Grants CHE-1808539 and DMR-1352328. Materials characterization was conducted at MAIC and NRF, College of Engineering Research Service Centers, University of Florida. W.G. especially appreciates the support of a graduate school fellowship from the University of Florida. A.A. gratefully acknowledges funding from National Science Foundation under Grant CHE-2002950.

#### **REFERENCES**

- (1) Tang, H.; Chen, C. J.; Huang, Z.; Bright, J.; Meng, G.; Liu, R. S.; Wu, N. Plasmonic hot electrons for sensing, photodetection, and solar energy applications: A perspective. *J. Chem. Phys.* 2020, *152*, 220901.
- (2) Gieseking, R. L.; Ratner, M. A; Schatz, G. C. Review of Plasmon-Induced Hot-Electron Dynamics and Related SERS Chemical ERects. In *Frontiers of Plasmon Enhanced Spectroscopy*, Vol. 1; Ozaki, Y., Schatz, G. C., Graham, D., Itoh, T., Eds.; American Chemical Society: Washington, DC, 2016; Chapter 1, pp 1–22.
- (3) Linic, S.; Aslam, U.; Boerigter, C.; Morabito, M. Photochemical transformations on plasmonic metal nanoparticles. *Nat. Mater.* 2015, 14, 567–576.
- (4) Aslam, U.; Rao, V. G.; Chavez, S.; Linic, S. Catalytic conversion of solar to chemical energy on plasmonic metal nanostructures. *Nat. Catal.* 2018, *1*,656–665.
- (5) Negrín-Montecelo, Y.; Movsesyan, A.; Gao, J.; Burger, S.; Wang, Z. M.; Nlate, S.; Pouget, E.; Oda, R.; Comesan □a-Hermo, M.; Govorov, A. O.; Correa-Duarte, M. A. Chiral generation of hot carriers for polarization-sensitive plasmonic photocatalysis. *J. Am. Chem. Soc.* 2022, 144, 1663–1671.
- (6) da Silva, A. G.; Rodrigues, T. S.; Wang, J.; Camargo, P. H. Plasmonic catalysis with designer nanoparticles. *ChemComm* 2022, *58*, 2055–2074.
- (7) Meng, X.; Liu, L.; Ouyang, S.; Xu, H.; Wang, D.; Zhao, N.; Ye, J. Nanometals for Solar-to-Chemical Energy Conversion: From Semi-conductor-Based Photocatalysis to Plasmon-Mediated Photocatalysis and Photo-Thermocatalysis. *Adv. Mater.* 2016, *28*, 6781–6803.
- (8) Zhou, L.; Swearer, D. F.; Zhang, C.; Robatjazi, H.; Zhao, H.; Henderson, L.; Dong, L.; Christopher, P.; Carter, E. A.; Halas, N. J.; et al. Quantifying hot carrier and thermal contributions in plasmonic photocatalysis. *Science* 2019, *362* (6410), 69–72.
- (9) Bayles, A.; Tian, S.; Zhou, J.; Yuan, L.; Yuan, Y.; Jacobson, C. R.; Farr, C.; Zhang, M.; Swearer, D. F.; Solti, D.; Lou, M.; Everitt, H. O.; Nordlander, P.; Halas, N. J. Al@TiO<sub>2</sub> Core-Shell Nanoparticles for Plasmonic Photocatalysis. *ACS Nano* 2022, *16*, 5839–5850.
- (10) Zhou, L.; Martirez, J. M. P.; Finzel, J.; Zhang, C.; Swearer, D. F.; Tian, S.; Robatjazi, H.; Lou, M.; Dong, L.; Henderson, L.; Christopher, P.; Carter, E. A.; Nordlander, P.; Halas, N. J. Light-driven methane dry reforming with single atomic site antenna-reactor plasmonic photocatalysts. *Nat. Energy* 2020, *5*, 61–70.

- (11) Zhang, P.; Wang, T.; Gong, J. Mechanistic Understanding of the Plasmonic Enhancement for Solar Water Splitting. *Adv. Mater.* 2015, *27*, 5328–5342.
- (12) Hu, C.; Chen, X.; Jin, J.; Han, Y.; Chen, S.; Ju, H.; Cai, J.; Qiu, Y.; Gao, C.; Wang, C.; Qi, Z.; Long, R.; Song, L.; Liu, Z.; Xiong, Y. Surface Plasmon Enabling Nitrogen Fixation in Pure Water through a Dissociative Mechanism under Mild Conditions. *J. Am. Chem. Soc.* 2019, *141*, 7807–7814.
- (13) Mubeen, S.; Lee, J.; Singh, N.; Kramer, S.; Stucky, G. D.; Moskovits, M. An Autonomous Photosynthetic Device in Which All Charge Carriers Derive from Surface Plasmons. *Nat. Nanotechnol.* 2013, *8*, 247–251.
- (14) Zhu, M.; Cai, X.; Fujitsuka, M.; Zhang, J.; Majima, T. Au/La<sub>2</sub>Ti<sub>2</sub>O<sub>7</sub> Nanostructures Sensitized with Black Phosphorus for Plasmon-Enhanced Photocatalytic Hydrogen Production in Visible and Near-Infrared Light. *Angew. Chemie Int. Ed.* 2017, *56*, 2064–2068.
- (15) Qian, K.; Sweeny, B. C.; Johnston-Peck, A. C.; Niu, W.; Graham, J. O.; Duchene, J. S.; Qiu, J.; Wang, Y.; Engelhard, M. H.; Su, D.; Stach, E. A.; Wei, D. W. Surface plasmon-driven water reduction: Gold nanoparticle size matters. *J. Am. Chem. Soc.* 2014, *136*, 9842–9845.
- (16) Jiang, W.; Bai, S.; Wang, L.; Wang, X.; Yang, L.; Li, Y.; Liu, D.; Wang, X.; Li, Z.; Jiang, J.; Xiong, Y. Integration of Multiple Plasmonic and Co-Catalyst Nanostructures on TiO<sub>2</sub> Nanosheets for Visible-Near-Infrared Photocatalytic Hydrogen Evolution. *Small* 2016, *12*, 1640–1648
- (17) Ingram, D. B.; Linic, S. Water Splitting on Composite Plasmonic-Metal/Semiconductor Photoelectrodes: Evidence for Selective Plasmon-Induced Formation of Charge Carriers near the Semiconductor Surface. *J. Am. Chem. Soc.* 2011, *133*, 5202–5205.
- (18) Cai, X.; Zhu, M.; Elbanna, O. A.; Fujitsuka, M.; Kim, S.; Mao, L.; Zhang, J.; Majima, T. Au Nanorod Photosensitized La<sub>2</sub>Ti<sub>2</sub>O<sub>7</sub> Nanosteps: Successive Surface Heterojunctions Boosting Visible to Near-Infrared Photocatalytic H<sub>2</sub> Evolution. *ACS Catal.* 2018, *8*, 122–131.
- (19) Li, R.; Cheng, W. H.; Richter, M. H.; DuChene, J. S.; Tian, W.; Li, C.; Atwater, H. A. Unassisted highly selective gas-phase CO<sub>2</sub> reduction with a plasmonic Au/p-GaN photocatalyst using H<sub>2</sub>O as an electron donor. *ACS Energy Lett.* 2021, *6*, 1849–1856.
- (20) Feng, K.; Wang, S.; Zhang, D.; Wang, L.; Yu, Y.; Feng, K.; Li, Z.; Zhu, Z.; Li, C.; Cai, M.; Wu, Z.; Kong, N.; Yan, B.; Zhong, J.; Zhang, X.; Ozin, G. A.; He, L. Cobalt Plasmonic Superstructures Enable Almost 100% Broadband Photon Efficient CO<sub>2</sub> Photocatalysis. *Adv. Mater.* 2020, *32* (24), 2000014.
- (21) Hou, W.; Hung, W. H.; Pavaskar, P.; Goeppert, A.; Aykol, M.; Cronin, S. B. Photocatalytic conversion of CO<sub>2</sub> to hydrocarbon fuels via plasmon-enhanced absorption and metallic interband transitions. *ACS Catal.* 2011, *1*, 929–936.
- (22) Collado, L.; Reynal, A.; Fresno, F.; Barawi, M.; Escudero, C.; Perez-Dieste, V.; Coronado, J. M.; Serrano, D. P.; Durrant, J. R.; de la Pena O'Shea, V. A. Unravelling the effect of charge dynamics at the plasmonic metal/semiconductor interface for CO<sub>2</sub> photoreduction. *Nat. Commun.* 2018, 9 (1), 4986.
- (23) Jia, H.; Du, A.; Zhang, H.; Yang, J.; Jiang, R.; Wang, J.; Zhang, C. Y. Site-Selective Growth of Crystalline Ceria with Oxygen Vacancies on Gold Nanocrystals for Near-Infrared Nitrogen Photofixation. *J. Am. Chem. Soc.* 2019, *141*, 5083–5086.
- (24) Li, C.; Wang, T.; Zhao, Z. J.; Yang, W.; Li, J. F.; Li, A.; Yang, Z.; Ozin, G. A.; Gong, J. Promoted Fixation of Molecular Nitrogen with Surface Oxygen Vacancies on Plasmon-Enhanced TiO<sub>2</sub> Photoelectrodes. *Angew. Chemie Int. Ed.* 2018, *57*, 5278–5282.
- (25) Yang, J.; Guo, Y.; Jiang, R.; Qin, F.; Zhang, H.; Lu, W.; Wang, J.; Yu, J. C. High-Efficiency 'working-in-Tandem' Nitrogen Photofixation Achieved by Assembling Plasmonic Gold Nanocrystals on Ultrathin Titania Nanosheets. *J. Am. Chem. Soc.* 2018, *140*, 8497–8508.

- (26) Wu, K.; Chen, J.; McBride, J. R.; Lian, T. Efficient Hot-Electron Transfer by a Plasmon-Induced Interfacial Charge-Transfer Transition. *Science* 2015, 349, 632–635.
- (27) Clavero, C. Plasmon-induced hot-electron generation at nanoparticle/metal-oxide interfaces for photovoltaic and photocatalytic devices. *Nat. Photonics* 2014, *8*, 95–103.
- (28) Park, J. Y.; Baker, L. R.; Somorjai, G. A. Role of Hot Electrons and Metal-Oxide Interfaces in Surface Chemistry and Catalysis. *Chem. Rev.* 2015, *115*, 2781–2817.
- (29) Zhang, Y.; He, S.; Guo, W.; Hu, Y.; Huang, J.; Mulcahy, J. R.; Wei, W. D. Surface-Plasmon-Driven Hot Electron Photochemistry. *Chem. Rev.* 2018, *118*, 2927–2954.
- (30) Lee, S. A.; Ostovar, B.; Landes, C. F.; Link, S. Spectroscopic signatures of plasmon-induced charge transfer in gold nanorods. *J. Chem. Phys.* 2022, *156*, 064702.
- (31) Wang, S.; Gao, Y.; Miao, S.; Liu, T.; Mu, L.; Li, R.; Fan, F.; Li, C. Positioning the Water Oxidation Reaction Sites in Plasmonic Photocatalysts. *J. Am. Chem. Soc.* 2017, *139*, 11771–11778.
- (32) Zeng, B.; Wang, S.; Gao, Y.; Li, G.; Tian, W.; Meeprasert, J.; Li, H.; Xie, H.; Fan, F.; Li, R.; Li, C. Interfacial Modulation with Aluminum Oxide for Efficient Plasmon-Induced Water Oxidation. *Adv. Funct. Mater.* 2021, *31*, 2005688.
- (33) Moon, S. Y.; Song, H. C.; Gwag, E. H.; Nedrygailov, I. I.; Lee, C.; Kim, J. J.; Doh, W. H.; Park, J. Y. Plasmonic hot carrier-driven oxygen evolution reaction on Au nanoparticles/TiO<sub>2</sub> nanotube arrays. *Nanoscale* 2018, *10*,22180–22188.
- (34) Zhang, Y.; Guo, W.; Zhang, Y.; Wei, W. D. Plasmonic Photoelectrochemistry: In View of Hot Carriers. *Adv. Mater.* 2021, *33*, 2006654.
- (35) Teranishi, M.; Wada, M.; Naya, S. I.; Tada, H. Size-Dependence of the Activity of Gold Nanoparticle-Loaded Titanium-(IV) Oxide Plasmonic Photocatalyst for Water Oxidation. *Chem-PhysChem* 2016, *17* (18), 2813–2817.
- (36) Shi, X.; Ueno, K.; Takabayashi, N.; Misawa, H. Plasmonenhanced photocurrent generation and water oxidation with a gold nanoisland-loaded titanium dioxide photoelectrode. *J. Phys. Chem. C* 2013, *117*, 2494–2499.
- (37) Primo, A.; Marino, T.; Corma, A.; Molinari, R.; García, H. Efficient visible-light photocatalytic water splitting by minute amounts of gold supported on nanoparticulate CeO<sub>2</sub> obtained by a biopolymer templating method. *J. Am. Chem. Soc.* 2011, *133*, 6930–6933.
- (38) Suzuki, K.; Li, X.; Toda, T.; Nagasawa, F.; Murakoshi, K. Plasmon-Accelerated Water Oxidation at Ni-Modified Au Nano-dimers on TiO<sub>2</sub> Single Crystals. *ACS Energy Lett.* 2021, 6, 4374–4382.
- (39) Shi, X.; Li, X.; Toda, T.; Oshikiri, T.; Ueno, K.; Suzuki, K.; Murakoshi, K.; Misawa, H. Interfacial Structure-Modulated Plasmon-Induced Water Oxidation on Strontium Titanate. *ACS Appl. Energy Mater.* 2020, *3*, 5675–5683.
- (40) Hung, S. F.; Xiao, F. X.; Hsu, Y. Y.; Suen, N. T.; Yang, H. B.; Chen, H. M.; Liu, B. Iridium Oxide-Assisted Plasmon-Induced Hot Carriers: Improvement on Kinetics and Thermodynamics of Hot Carriers. *Adv. Energy Mater.* 2016, 6 (8), 1501339.
- (41) Gao, Y.; Cheng, F.; Fang, W.; Liu, X.; Wang, S.; Nie, W.; Chen, R.; Ye, S.; Zhu, J.; An, H.; Fan, C.; Fan, F.; Li, C. Probing of coupling effect induced plasmonic charge accumulation for water oxidation. *Natl. Sci. Rev.* 2021, *8* (6), nwaa151.
- (42) Li, H.; Wang, S.; Wang, M.; Gao, Y.; Tang, J.; Zhao, S.; Chi, H.; Zhang, P.; Qu, J.; Fan, F.; Li, C. Enhancement of Plasmon-Induced Photoelectrocatalytic Water Oxidation over Au/TiO<sub>2</sub> with Lithium Intercalation. *Angew. Chem., Int. Ed.* 2022, *61* (30), No. e202204272.
- (43) Huang, J.; He, S.; Goodsell, J. L.; Mulcahy, J. R.; Guo, W.; Angerhofer, A.; Wei, W. D. Manipulating Atomic Structures at the Au/TiO<sub>2</sub> Interface for O<sub>2</sub> Activation. *J. Am. Chem. Soc.* 2020, 142, 6456–6460.
- (44) He, S.; Huang, J.; Goodsell, J. L.; Angerhofer, A.; Wei, W. D. Plasmonic Nickel-TiO<sub>2</sub> Heterostructures for Visible-Light-Driven Photochemical Reactions. *Angew. Chem., Int. Ed.* 2019, *58*, 6038–6041.

- (45) Mukherjee, S.; Zhou, L.; Goodman, A. M.; Large, N.; Ayala-Orozco, C.; Zhang, Y.; Nordlander, P.; Halas, N. J. Hot-Electron-Induced Dissociation of H<sub>2</sub> on Gold Nanoparticles Supported on SiO<sub>2</sub>. *J. Am. Chem. Soc.* 2014, *136*, 64–67.
- (46) CRC Handbook of Chemistry and Physics; CRC Press, Taylor & Francis [distributor]: Boca Raton, FL, London, UK, 2008.
- (47) Bernardi, M.; Mustafa, J.; Neaton, J. B.; Louie, S. G. Theory and computation of hot carriers generated by surface plasmon polaritons in noble metals. *Nat. Commun.* 2015, *6* (1), 7044.
- (48) Bard, A. J. Inner-sphere heterogeneous electrode reactions. Electrocatalysis and photocatalysis: the challenge. *J. Am. Chem. Soc.* 2010, *132*, 7559–7567.
- (49) Eisenberg, M.; Silverman, H. P. Photo-Electrochemical Cells. Electrochem. *Acta* 1961, 5, 1–12.
- (50) Siemer, N.; Lu ken, A.; Zalibera, M.; Frenzel, J.; MrLz-Santiburcio, D.; Savitsky, A.; Lubitz, W.; Muhler, M.; Marx, D.; Strunk, J. Atomic-Scale Explanation of O<sub>2</sub> Activation at the Au-TiO<sub>2</sub> Interface. *J. Am. Chem. Soc.* 2018, *140*, 18082–18092.
- (51) Priebe, J. B.; Radnik, J.; Lennox, A. J. J.; Pohl, M.; Karnahl, M.; Hollmann, D.; Grabow, K.; Bentrup, U.; Junge, H.; Beller, M.; Bru ckner, A. Solar Hydrogen Production by Plasmonic Au-TiO<sub>2</sub> Catalysts: Impact of Synthesis Protocol and TiO<sub>2</sub> Phase on Charge Transfer Efficiency and H<sub>2</sub> Evolution Rates. *ACS Catal.* 2015, *5*, 2137–2148.
- (52) Priebe, J. B.; Karnahl, M.; Junge, H.; Beller, M.; Hollmann, D.; Bru ckner, A. Water Reduction with Visible Light: Synergy between Optical Transitions and Electron Transfer in Au-TiO<sub>2</sub> Catalysts Visualized by in Situ EPR Spectroscopy. *Angew. Chem., Int. Ed.* 2013, 52, 11420–11424.
- (53) Ke, S. C.; Wang, T. C.; Wong, M. S.; Gopal, N. O. Low temperature kinetics and energetics of the electron and hole traps in irradiated TiO<sub>2</sub> nanoparticles as revealed by EPR spectroscopy. *J. Phys. Chem. B* 2006, *110*, 11628–11634.
- (54) Hurum, D. C.; Agrios, A. G.; Gray, K. A.; Rajh, T.; Thurnauer, M. C. Explaining the enhanced photocatalytic activity of Degussa P25 mixed-phase TiO<sub>2</sub> using EPR. *J. Phys. Chem. B* 2003, *107*, 4545–4549.
- (55) Dimitrijevic, N. M.; Vijayan, B. K.; Poluektov, O. G.; Rajh, T.; Gray, K. A.; He, H.; Zapol, P. Role of water and carbonates in photocatalytic transformation of CO<sub>2</sub> to CH<sub>4</sub> on titania. *J. Am. Chem. Soc.* 2011, *133*, 3964–3971.
- (56) Chiesa, M.; Paganini, M. C.; Livraghi, S.; Giamello, E. Charge trapping in TiO<sub>2</sub> polymorphs as seen by Electron Paramagnetic Resonance spectroscopy. *Phys. Chem. Chem. Phys.* 2013, *15* (24), 9435–9447.
- (57) Pan, X.; Yang, M. Q.; Fu, X.; Zhang, N.; Xu, Y. J. Defective TiO<sub>2</sub> with oxygen vacancies: Synthesis, properties and photocatalytic applications. *Nanoscale* 2013, 5, 3601–3614.
- (58) Carter, E.; Carley, A. F.; Murphy, D. M. Evidence for O<sub>2</sub><sup>-</sup> radical stabilization at surface oxygen vacancies on polycrystalline TiO<sub>2</sub>. *J. Phys. Chem. C* 2007, *111*, 10630–10638.
- (59) Li, H.; Wang, S.; Hong, F.; Gao, Y.; Zeng, B.; Haider, R. S.; Fan, F.; Huang, J.; Li, C. Effects of the interfacial defects in Au/TiO<sub>2</sub> on plasmon-induced water oxidation. *J. Chem. Phys.* 2020, *152*, 194702.
- (60) Nakamura, I.; Negishi, N.; Kutsuna, S.; Ihara, T.; Sugihara, S.; Takeuchi, K. Role of oxygen vacancy in the plasma-treated TiO<sub>2</sub> photocatalyst with visible light activity for NO removal. *J. Mol. Catal. A Chem.* 2000, *161*, 205–212.
- (61) Sun, Y.; Egawa, T.; Shao, C.; Zhang, L.; Yao, X. EPR line broadening of F center in high-surface-area anatase titania nanoparticles prepared by MOCVD. *J. Cryst. Growth* 2004, *268*,118–122.
- (62) Tagliabue, G.; Jermyn, A. S.; Sundararaman, R.; Welch, A. J.; DuChene, J. S.; Pala, R.; Davoyan, A. R.; Narang, P.; Atwater, H. A. Quantifying the role of surface plasmon excitation and hot carrier transport in plasmonic devices. *Nat. Commun.* 2018, *9* (1), 3394.
- (63) Khurgin, J. B. How to deal with the loss in plasmonics and metamaterials. *Nat. Nanotechnol.* 2015, 10,2–6.

- (64) Liu, L.; Li, P.; Adisak, B.; Ouyang, S.; Umezawa, N.; Ye, J.; Kodiyath, R.; Tanabe, T.; Ramesh, G. V.; Ueda, S.; Abe, H. Gold photosensitized SrTiO₃ for visible-light water oxidation induced by Au interband transitions. *J. Mater. Chem. A* 2014, *2*, 9875–9882.
- (65) Meng, X.; Yu, Q.; Wang, T.; Liu, G.; Chang, K.; Li, P.; Liu, L.; Ye, J. Exceptional enhancement of H<sub>2</sub> production in alkaline environment over plasmonic Au/TiO<sub>2</sub> photocatalyst under visible light. *APL Mater.* 2015, *3*, 104401.
- (66) Brown, A. M.; Sundararaman, R.; Narang, P.; Goddard, W. A.; Atwater, H. A. Nonradiative plasmon decay and hot carrier dynamics: Effects of phonons, surfaces, and geometry. *ACS Nano* 2016, *10*, 957–966.
- (67) Duchene, J. S.; Tagliabue, G.; Welch, A. J.; Cheng, W. H.; Atwater, H. A. Hot Hole Collection and Photoelectrochemical CO<sub>2</sub> Reduction with Plasmonic Au/p-GaN Photocathodes. *Nano Lett.* 2018, *18*, 2545–2550.
- (68) Naik, G. V.; Welch, A. J.; Briggs, J. A.; Solomon, M. L.; Dionne, J. A. Hot-Carrier-Mediated Photon Upconversion in Metal-Decorated Quantum Wells. *Nano Lett.* 2017, *17*, 4583–4587.
- (69) Micic, O. I.; Zhang, Y.; Cromack, K. R.; Trifunac, A. D.; Thurnauer, M. C. Trapped holes on titania colloids studied by electron paramagnetic resonance. *J. Phys. Chem.* 1993, 97, 7277–7283.
- (70) Zhang, Y.; Zhang, Y.; Guo, W.; Johnston-Peck, A. C.; Hu, Y.; Song, X.; Wei, W. D. Modulating multi-hole reaction pathways for photoelectrochemical water oxidation on gold nanocatalysts. *Energy Environ. Sci.* 2020, *13*, 1501–1508.
- (71) Kim, Y.; Smith, J. G.; Jain, P. K. Harvesting multiple electronhole pairs generated through plasmonic excitation of Au nanoparticles. *Nat. Chem.* 2018, *10*, 763–769.
- (72) Yu, S.; Jain, P. K. Isotope effects in plasmonic photosynthesis. *Angew. Chemie Int. Ed.* 2020, **59**, 22480–22483.
- (73) Kim, Y.; Dumett Torres, D.; Jain, P. K. Activation energies of plasmonic catalysts. *Nano Lett.* 2016, 16, 3399–3407.
- (74) Yu, S.; Wilson, A. J.; Heo, J.; Jain, P. K. Plasmonic control of multi-electron transfer and C-C coupling in visible-light-driven CO<sub>2</sub> reduction on Au nanoparticles. *Nano Lett.* 2018, *18*, 2189–2194.
- (75) Stoll, S.; Schweiger, A. EasySpin, a comprehensive software package for spectral simulation and analysis in EPR. *J. Magn. Reson.* 2006, *178*, 42–55.

# Elucidating the Origin of Plasmon-Generated Hot Holes in Water Oxidation

Jiawei Huang, Wenxiao Guo, Shuai He, Justin R. Mulcahy, Alvaro Montoya, Justin Goodsell, Namodhi Wijerathne, Alexander Angerhofer, and Wei David Wei<sup>\*</sup>

Department of Chemistry and Center for Catalysis, University of Florida, Gainesville, Florida 32611, United States.

E-mail: wei@chem.ufl.edu

Materials. Commercially available P25 (Degussa) and methanol (99.8%) were purchased from Fisher Scientific (Hampton, NH). Chloroauric acid trihydrate (HAuCl₄•3H₂O) (≥99.9% trace metals basis), silica (SiO₂) (100-200 mesh silica gel), and ammonium hydroxide (NH₄OH) (ACS reagent, 28.0–30.0% NH₃ basis) were purchased from Sigma-Aldrich (St. Louis, MO). All chemicals were used as received without further purification. All glassware was cleaned with aqua regia solution, followed by copious rinsing with Nanopure™ H₂O (Barnstead, 18.2 MΩ cm) prior to use. (CAUTION! Aqua regia is highly corrosive and toxic. Handle with care and use appropriate personal protective equipment.)

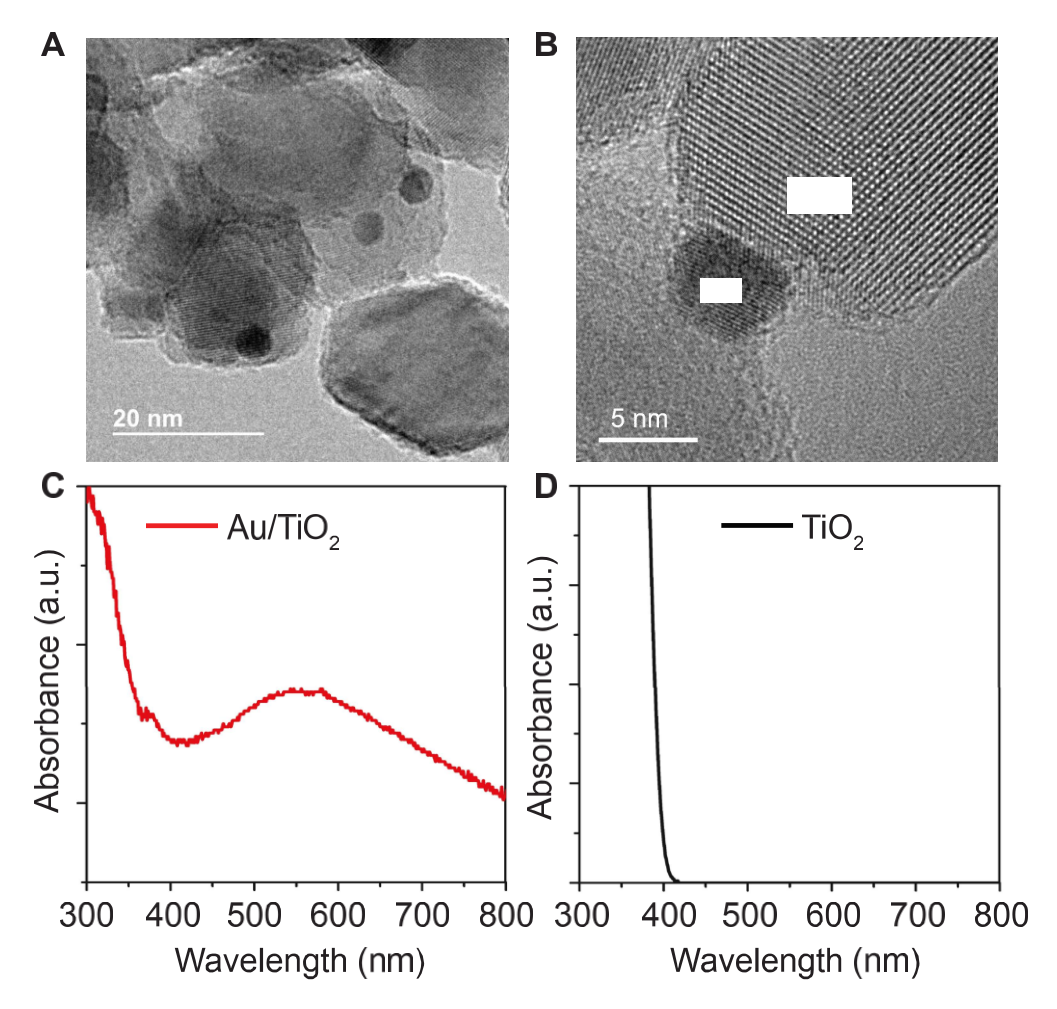


Figure S1. Characterization of Au/TiO<sub>2</sub> heterostructures prepared by the deposition-precipitation method. (A) TEM image of Au/TiO<sub>2</sub> heterostructures. The size of Au NPs is  $4.3 \pm 0.6$  nm. (B) HRTEM of Au/TiO<sub>2</sub> heterostructures, showing that a heterogeneous interface has been constructed between Au and TiO<sub>2</sub>. UV-Vis spectrum of (C) Au/TiO<sub>2</sub> heterostructures and (D) bare TiO<sub>2</sub>. For Au/TiO<sub>2</sub> heterostructures, the localized surface plasmon resonance (LSPR) arising from Au NPs is found to be approximately 556 nm.

Further Discussions about Plasmon-Driven Water Oxidation on Au/TiO<sub>2</sub> and Au/SiO<sub>2</sub> Heterostructures. The observation of continuous oxygen evolution on Au/TiO<sub>2</sub> heterostructures and the inactive water oxidation on Au/SiO<sub>2</sub> heterostructures upon LSPR excitation was consistent with previous studies. A mechanism of water nucleophilic attack (WNA) to -Ti-O species to form an O-O bond was proposed for the water oxidation (Figure S2B). In detail, hot holes from the plasmon-assisted interband excitation in Au NPs were transferred to surface oxygen atoms of TiO<sub>2</sub> at the Au/TiO<sub>2</sub> interface. Thereafter, one hot hole from a nearby surface oxygen atom of TiO<sub>2</sub> deprotonated a water molecule adsorbed at the surface Ti atom to form a ·OH species (Step 1). The coupling between this ·OH species and the surface O- species (a hole accumulated at the surface oxygen atom of TiO<sub>2</sub>) further created the Ti-OOH species (Step 2). Eventually, O<sub>2</sub> molecules were released from the TiO<sub>2</sub> surface after the proton-coupled hole transfer process (Steps 3,4, and 5).

Previous studies have demonstrated that plasmon-generated hot electrons that remained on the surface of colloidal plasmonic metal NPs (e.g., Au and Ag) were capable to reduce Fe<sup>3+</sup> into Fe<sup>2+,6-</sup>

<sup>9</sup> Accordingly, for the water oxidation on Au/SiO<sub>2</sub> heterostructures, plasmon-generated hot electrons on Au NPs were consumed by the electron scavenger (i.e., Fe(NO<sub>3</sub>)<sub>3</sub>), leaving long-lived hot holes that were available to oxidize water molecules. The inactive water oxidation on Au/SiO<sub>2</sub> heterostructures suggested that hot holes on Au were thermodynamically unfavorable for driving the water oxidation reaction (approximately – 5.73 eV vs. vacuum)<sup>10,11</sup> since hot holes on Au NPs should quickly relax to the Au Fermi level (approximately – 5.1 eV vs. vacuum). <sup>12</sup> By comparison, on Au/TiO<sub>2</sub> heterostructures, plasmon-generated hot electron-hole pairs were more efficiently separated by the interfacial Schottky barrier, allowing more hot electrons to be consumed by Fe(NO<sub>3</sub>)<sub>3</sub> and leading to the accumulation of more hot holes on Au NPs. To exclude the possibility

that such large amounts of hot holes on  $TiO_2$ -supported Au NPs will shift the Fermi level of Au to an anodic direction and eventually make hot holes at Au Fermi level become thermodynamically favorable to oxidize water molecules, we characterized the size variation of Au NPs after the water oxidation. It should be noted that the hot-hole-induced Au etching process should have already occurred before hot holes on Au participate in the water oxidation reaction.<sup>13</sup> As shown in Figure S3, the size of Au NPs was  $5.7 \pm 0.9$  nm after the plasmon-driven water oxidation reaction, excluding the hot-hole-mediated Au etching process that should result in the smaller Au NPs as compared to the size of as-prepared Au NPs.

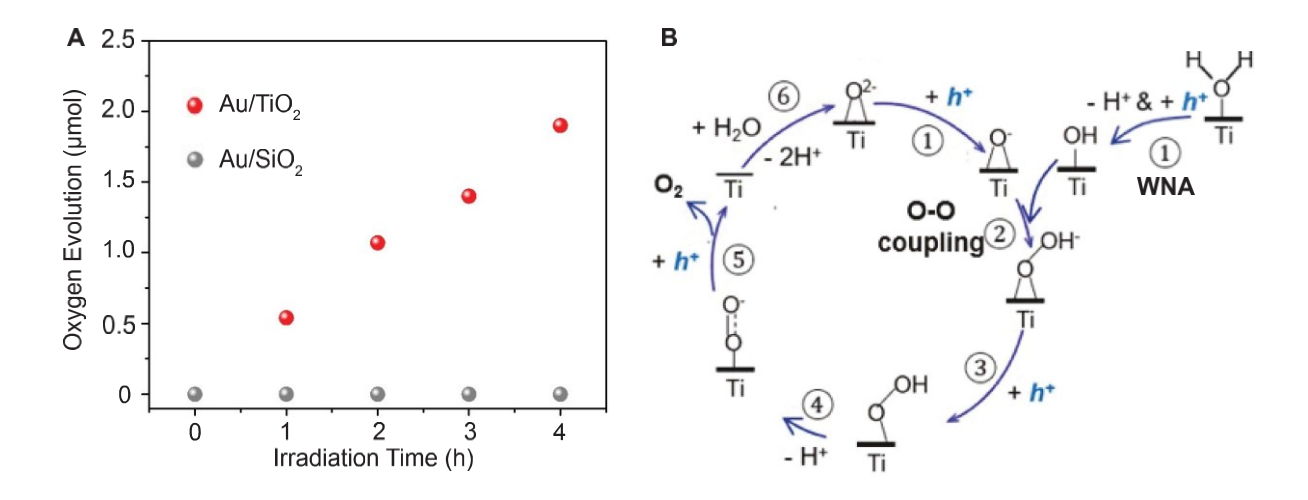


**Figure S2.** Hot-hole-driven water oxidation on Au/TiO<sub>2</sub> and Au/SiO<sub>2</sub> heterostructures. (A) Water oxidation reaction on Au/TiO<sub>2</sub> heterostructures (red) and Au/SiO<sub>2</sub> heterostructures (gray) under visible-light irradiation ( $\lambda > 495$  nm). (B) Reaction pathway of hot-hole-driven water oxidation reaction on Au/TiO<sub>2</sub> heterostructures.

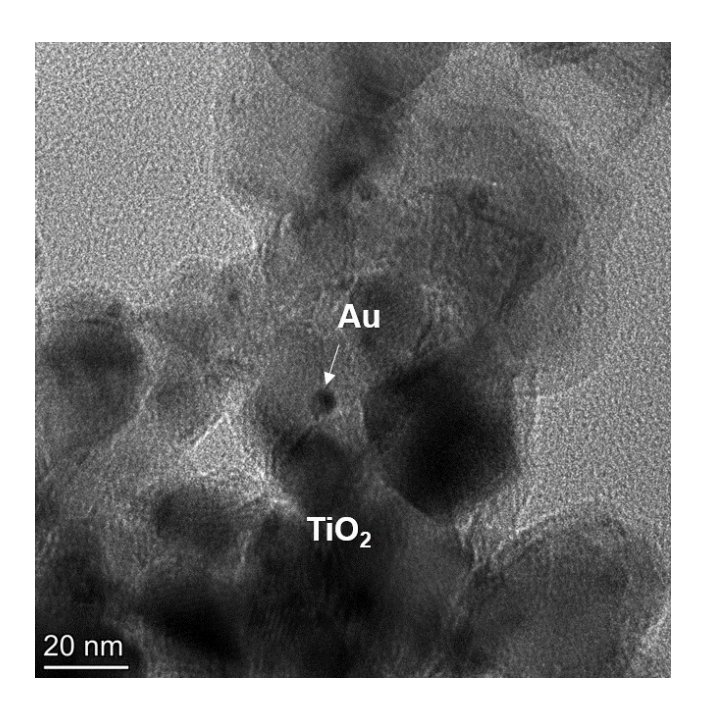
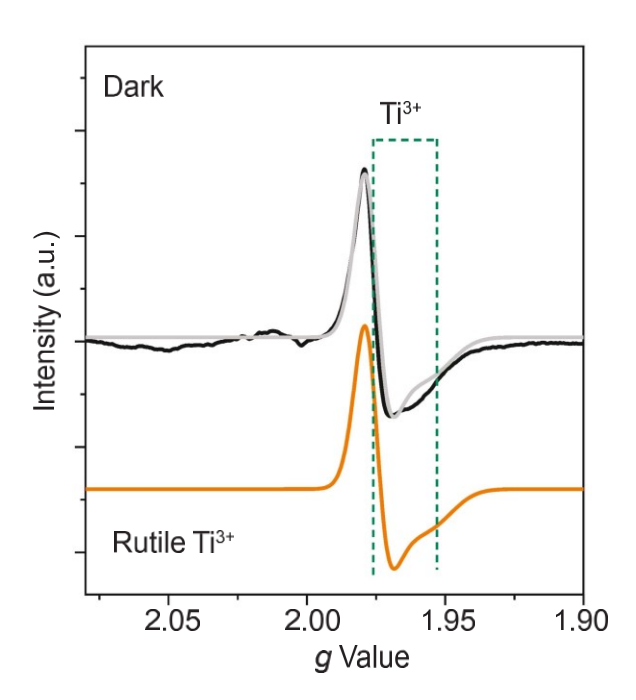


Figure S3. TEM characterization of Au/TiO<sub>2</sub> heterostructures after the plasmon-driven water oxidation reaction. The size of Au NPs is  $5.7 \pm 0.9$  nm.



**Figure S4.** Experimental (black) and simulated (gray) X-band EPR spectra of Au/TiO<sub>2</sub> heterostructures in the dark. The simulated spectrum (gray) is originated from electrons trapped at Ti<sup>3+</sup> species in the rutile TiO<sub>2</sub> phase (orange). Note: EPR spectrum was collected at 5 K in He condition and the EPR background spectrum has been subtracted from the initial spectrum.

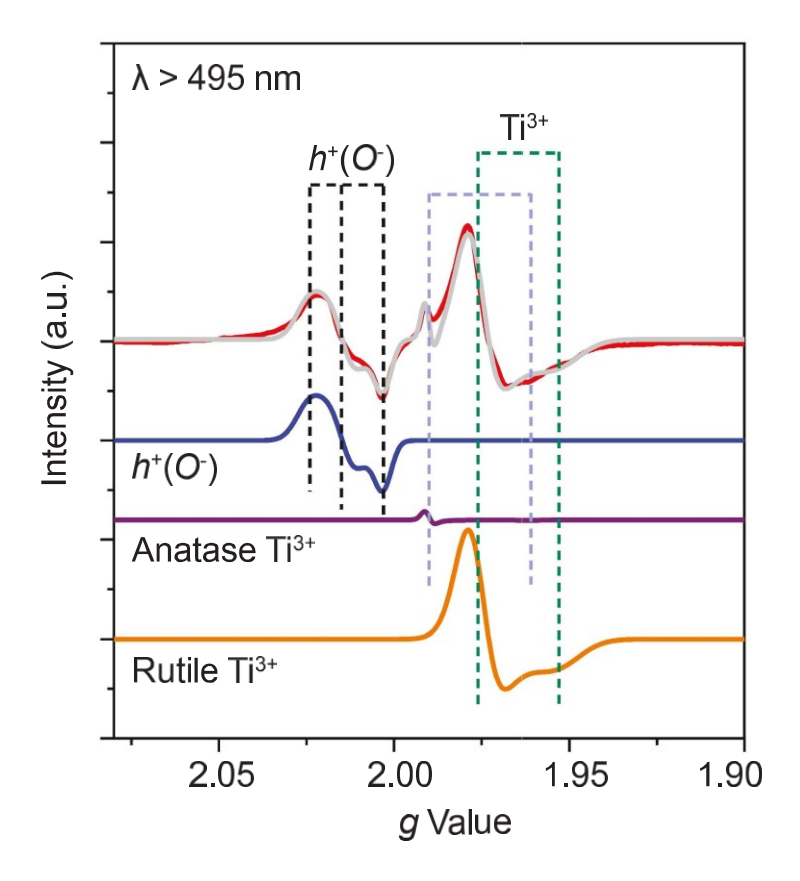
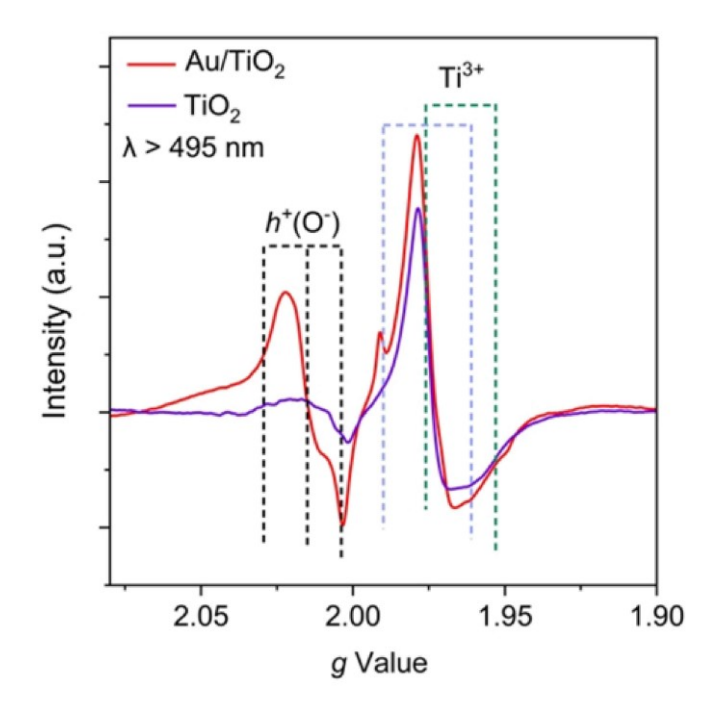
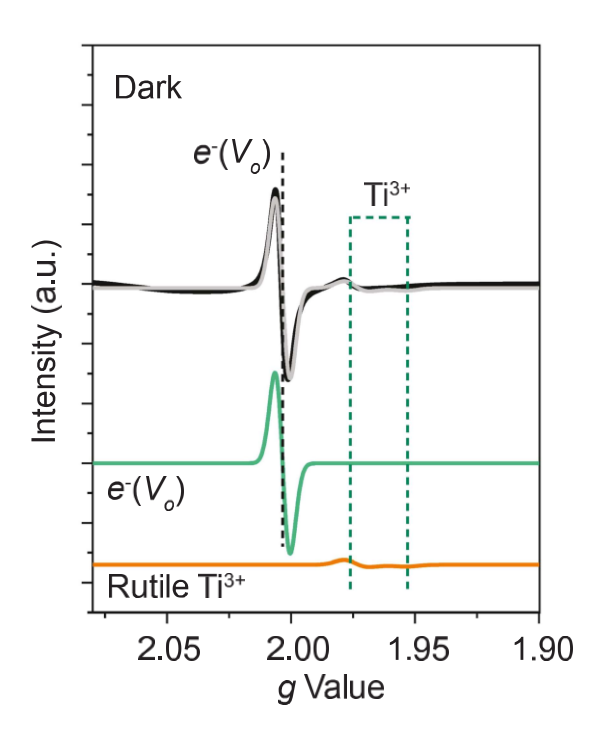


Figure S5. Experimental (red) and simulated (gray) X-band EPR spectra of Au/TiO<sub>2</sub> heterostructures under visible-light irradiation ( $\lambda > 495$  nm). The simulated spectrum (gray) can be further deconvoluted into various respective components, where  $h^+(O^-)$  (blue) represents hot holes stayed on surface oxygen atoms of TiO<sub>2</sub>, anatase Ti<sup>3+</sup> (purple) represents electrons trapped at Ti<sup>3+</sup> sites in the anatase TiO<sub>2</sub> phase, and rutile Ti<sup>3+</sup> (orange) is assigned to electrons trapped at Ti<sup>3+</sup> sites in the rutile TiO<sub>2</sub> phase.<sup>3,18–21</sup> Note: EPR spectrum was collected at 5 K in He condition and the EPR background spectrum has been subtracted from the initial spectrum.



**Figure S6.** *In situ* EPR spectra of Au/TiO<sub>2</sub> heterostructures and bare TiO<sub>2</sub> under visible-light irradiation ( $\lambda > 495$  nm) (red) at 5 K under He condition. Note: For Ti<sup>3+</sup> species, the light-blue and green lines represent *g* values of anatase Ti<sup>3+</sup> and rutile Ti<sup>3+</sup> species, respectively.

**Further Discussions about Formation of Oxygen Vacancies on TiO<sub>2</sub> using Photo-Deposition Method.** For Au/TiO<sub>2</sub> heterostructures prepared by the photo-deposition method, the EPR feature (g = 2.003) of electrons trapped at oxygen vacancies of TiO<sub>2</sub>  $(e^{-}(V_0))$  was observable in the dark (the black curve in Figure 2A and the corresponding simulation result in Figure S7), <sup>14,15</sup> showing that oxygen vacancies were created on TiO<sub>2</sub>. This was consistent with previous studies, which also reported that the photo-deposition method was able to create oxygen vacancies on TiO<sub>2</sub>. <sup>16,17</sup> During the photo-deposition synthesis, TiO<sub>2</sub> efficiently absorbed UV light, generating electron-hole pairs. The trapped holes on the TiO<sub>2</sub> surface weakened the binding strength between the Ti atom and the lattice oxygen of TiO<sub>2</sub>. With the assistance of methanol oxidation, lattice oxygen atoms were extracted from the TiO<sub>2</sub> surface, leading to the formation of surface oxygen vacancies on TiO<sub>2</sub>. <sup>16</sup>



**Figure S7.** Experimental (black) and simulated (gray) X-band EPR spectra of photo-deposition-prepared Au/TiO<sub>2</sub> heterostructures in the dark. The simulated spectrum (gray) can be further deconvoluted into various respective components, where  $e^{-}(V_0)$  with a g value of 2.003 represents the accumulation of electrons at oxygen vacancies of TiO<sub>2</sub> and Ti<sup>3+</sup> is originated from electrons accumulated at Ti centers of rutile TiO<sub>2</sub>. Note: EPR spectra were collected at 5 K in He condition, and the EPR background spectrum has been subtracted from the initial spectra.

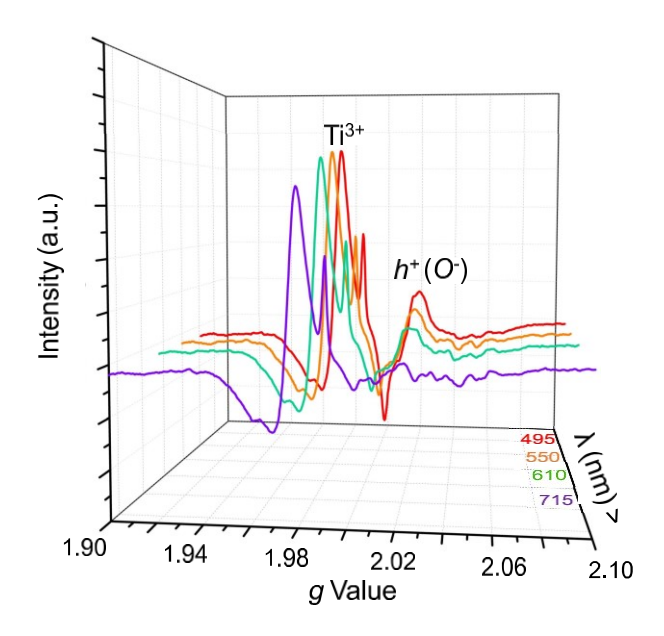


**Figure S8.** Three-dimensional X-band EPR spectra of Au/TiO<sub>2</sub> heterostructures under different irradiation wavelengths at 5 K under He condition. Note:  $h^+(O^-)$  represents the accumulation of hot holes on surface oxygen atoms of TiO<sub>2</sub> and Ti<sup>3+</sup> is attributable to electrons accumulated at Ti centers of TiO<sub>2</sub>. The EPR background spectrum has been subtracted from the initial spectra of Au/TiO<sub>2</sub> heterostructures.

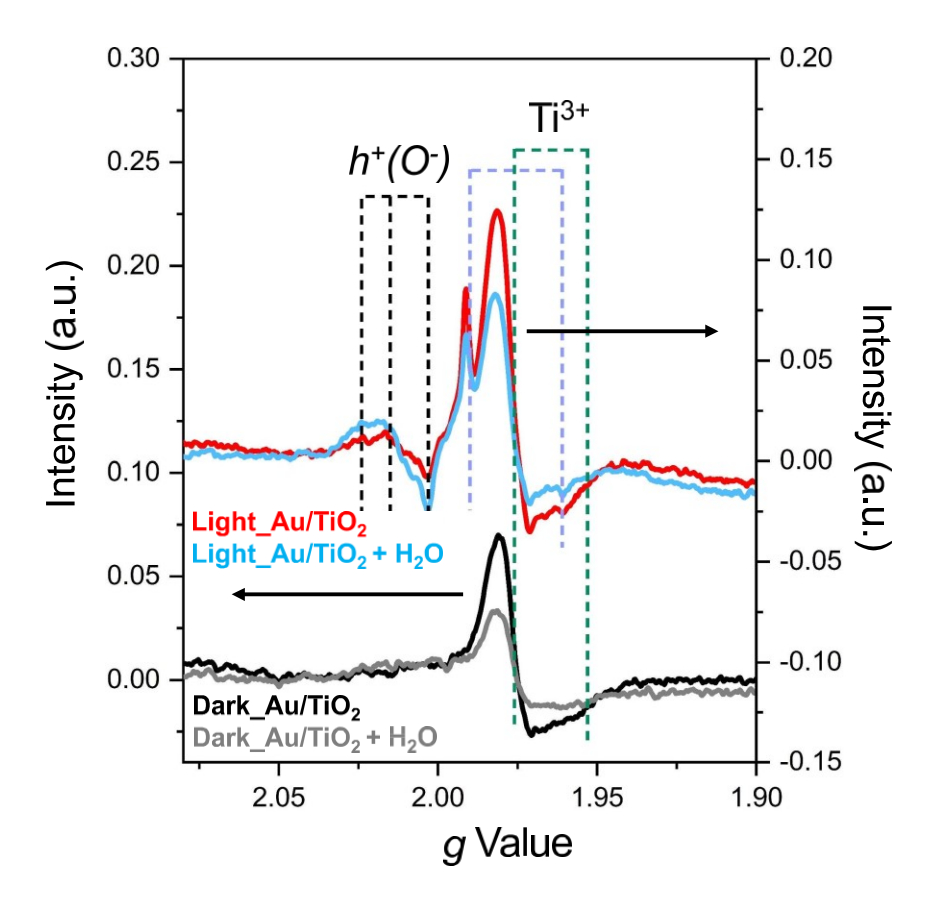


**Figure S9.** Initial X-band EPR spectra of Au/TiO<sub>2</sub> heterostructures before and after the addition of water molecules. For dried Au/TiO<sub>2</sub> heterostructures, the dark and visible-light irradiation ( $\lambda > 495$  nm) EPR spectra are shown in the black and red curves, respectively. For Au/TiO<sub>2</sub> heterostructures in the presence of water molecules, the dark and visible-light irradiation ( $\lambda > 495$  nm) EPR spectra are shown in the gray and blue curves, respectively. Note:  $h^+(O^-)$  represents the accumulation of hot holes on surface oxygen atoms of TiO<sub>2</sub> and Ti<sup>3+</sup> is attributable to electrons accumulated at Ti centers of TiO<sub>2</sub>. For Ti<sup>3+</sup> species, the light-blue and green lines represent g values of anatase Ti<sup>3+</sup> and rutile Ti<sup>3+</sup> species, respectively. The EPR spectra were collected at 90 K, and the EPR background spectrum has been subtracted from the initial spectra.

It is noted that the addition of water molecules decreased the EPR signal of Ti<sup>3+</sup> feature in the dark condition (black and gray spectra in Figure S9). The water-induced decrease of Ti<sup>3+</sup> signal was attributable to the partial absorption of microwave by water molecules, reducing the incoming energy to trigger the spin excitation of unpaired electrons in Au/TiO<sub>2</sub> heterostructures. Similar water-induced Ti<sup>3+</sup> signal attenuation was also observable under visible light irradiation (red and

cyan spectra in Figure S9). Surprisingly, the EPR signal of  $h^+(O^-)$  species on Au/TiO<sub>2</sub> heterostructures increased after the introduction of water molecules, clearly demonstrating the formation of more  $O^-$  species due to the transfer of hot holes from Au/TiO<sub>2</sub> heterostructures to oxygen atoms of adsorbed water molecules to produce additional  $O^-$  species.

To eliminate the impact of water during EPR measurements and clearly highlight the intensity variation of visible-light-induced  $h^+(O^-)$  species on Au/TiO<sub>2</sub> heterostructures before and after the addition of water molecules, we adjusted the EPR spectrum of Au/TiO<sub>2</sub> heterostructures in the presence of water molecules in the dark (gray spectra in Figure S9) to the same intensity of EPR spectrum of dried Au/TiO<sub>2</sub> heterostructures in the dark condition (black spectra in Figure S9). Accordingly, as shown in Figure 5A, the intensity of the visible-light EPR spectrum of Au/TiO<sub>2</sub> heterostructures in the presence of water molecules (the blue spectrum in Figure S9) was also multiplied by the same factor in the alignment of dark EPR spectra.

In addition to the water-enhanced  $h^+(O^-)$  signal, it is noted that the presence of surface water also increased the EPR signal of  $Ti^{3+}$  feature in Au/TiO<sub>2</sub> heterostructures. It is proposed that the addition of water induces a shift of hole transfer equilibrium and allows more interband hot holes to be transferred from Au to  $TiO_2$ , suppressing the recombination of hot holes and hot electrons in Au. As a result, more hot electrons transfer to  $TiO_2$  and stay at Ti centers, resulting in the increase of  $Ti^{3+}$  EPR signal in the presence of water.

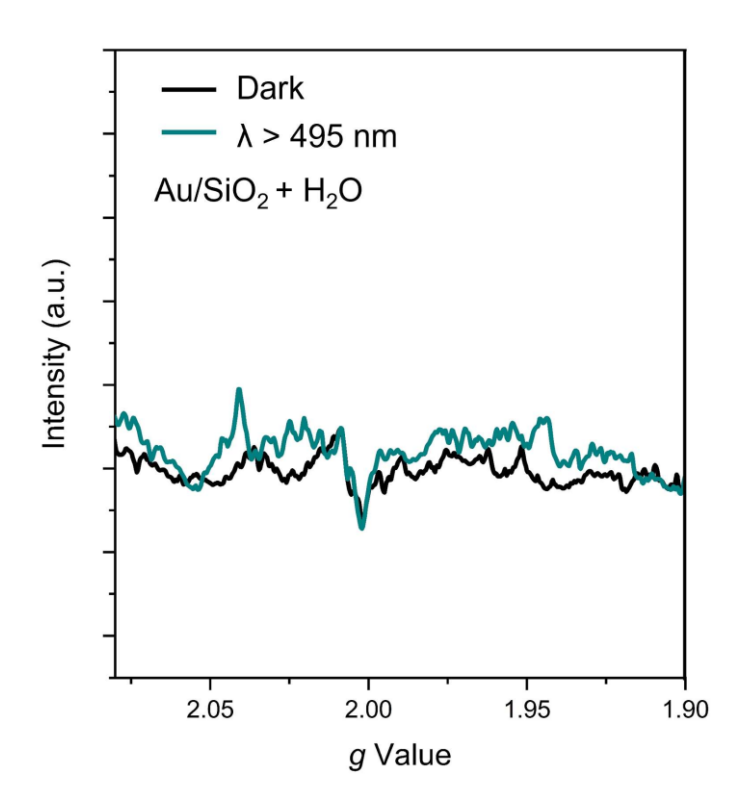


**Figure S10.** X-band EPR spectra of Au/SiO<sub>2</sub> heterostructures in the presence of water molecules. Only the background noise was observable on Au/SiO<sub>2</sub> heterostructures in the presence of water molecules both under the dark and visible-light irradiation ( $\lambda > 495$  nm), showing that holes that remained on Au NPs were unable to transfer to adsorbed water molecules to produce  $h^+(O^-)$  species. Note: The EPR spectra were collected at 90 K.

#### Chemical Descriptions about the Formation of O<sup>-</sup> Species from Water

In the presence of water, hydroxyl groups from water covalently bond to the surface Ti centers, transforming initial Ti-O<sup>-</sup> at the dried Au/TiO<sub>2</sub> interface to Ti-O<sup>-</sup>-Ti-OH<sup>-</sup> (O<sup>-</sup> in both Ti-O<sup>-</sup> and Ti-O<sup>-</sup>-Ti-OH<sup>-</sup> represents hot holes that stay on oxygen atoms of TiO<sub>2</sub>). After that, hot holes transfer from oxygen atoms of TiO<sub>2</sub> into hydroxyl groups of adsorbed water:

$$Ti-O^{-\bullet}-Ti-OH^{-} \rightarrow Ti-O^{2-}-Ti-O^{-\bullet}+H^{+}$$

where O<sup>-•</sup> in Ti-O<sup>2-</sup>-Ti-O<sup>-•</sup> represents the oxygen radicals in hydroxyl groups of adsorbed water molecules and O<sup>2-</sup> in Ti-O<sup>2-</sup>-Ti-O<sup>-•</sup> is the oxygen atom of TiO<sub>2</sub> once hot holes leave. Such hole

transfer from TiO<sub>2</sub> to hydroxyl groups of water molecules results in a shift of the hole equilibrium in Au/TiO<sub>2</sub>, leading to the transfer of additional interband hot holes from Au into TiO<sub>2</sub>:

$$Ti-O^2-Ti-O^{-\bullet} + h^+ \rightarrow Ti-O^{-\bullet}-Ti-O^{-\bullet}$$

where O<sup>-\*</sup> in Ti-O<sup>-\*</sup>-Ti-O<sup>-\*</sup>originate from both oxygen radicals in TiO<sub>2</sub> and hydroxyl group of adsorbed water molecules. Therefore, the addition of water to Au/TiO<sub>2</sub> produces more O<sup>-\*</sup> species as compared to the number of O<sup>-\*</sup> species only originating from TiO<sub>2</sub> in dried samples, resulting in the increase of the EPR signal for  $h^+(O^-)$  in the presence of water.

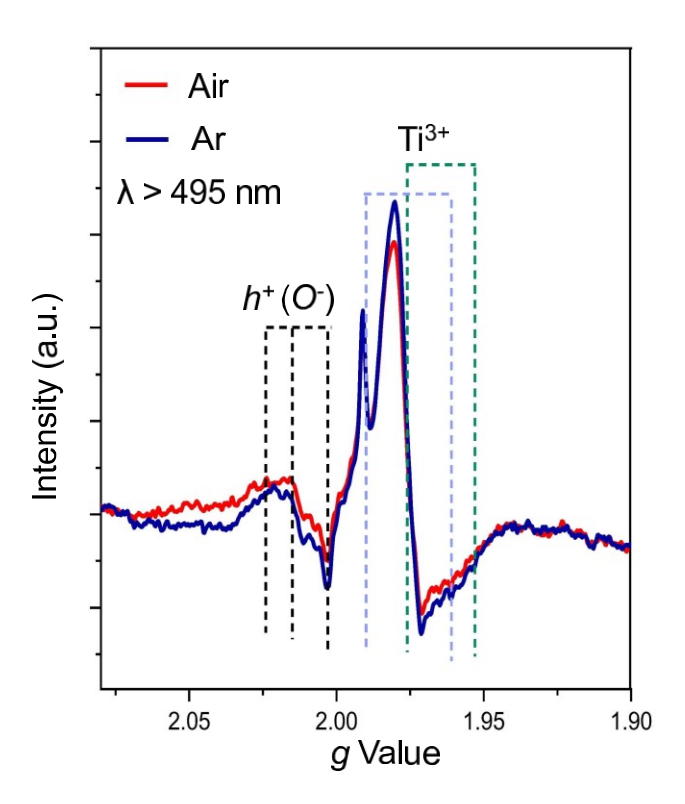


**Figure S11.** X-band EPR spectra of Au/TiO<sub>2</sub> heterostructures under air and Ar conditions at 90 K. Note:  $h^+(O^-)$  represents the accumulation of hot holes on surface oxygen atoms of TiO<sub>2</sub>. Ti<sup>3+</sup> represents electrons accumulated at Ti centers of TiO<sub>2</sub>. For Ti<sup>3+</sup> species, the light-blue and green lines represent g values of anatase Ti<sup>3+</sup> and rutile Ti<sup>3+</sup> species, respectively. The EPR background spectrum has been subtracted from the initial spectra.

**Table S1.** Summary of g values used for simulation of X-band EPR spectra. <sup>18–21</sup>

Signal Assignment	Average $g_x$	Average $g_y$	Average $g_z$
Rutile Ti <sup>3+</sup>	1.976	1.976	1.953
Anatase Ti <sup>3+</sup>	1.990	1.990	1.961
O <sub>2</sub> -	2.002	2.007	2.028
$h^+(\mathrm{O}^-)$	2.003	2.015	2.024
$e^{-}(V_{\rm o})$	2.003	2.003	2.003

#### References

- 1. Wang, S.; Gao, Y.; Miao, S.; Liu, T.; Mu, L.; Li, R.; Fan, F.; Li, C. Positioning the Water Oxidation Reaction Sites in Plasmonic Photocatalysts. *J. Am. Cher. Soc.* **2017**, 139, 11771–11778.
- 2. Zhang, Y.; Zhang, H.; Ji, H.; Ma, W.; Chen, C.; Zhao, J. Pivotal Role and Regulation of Proton Transfer in Water Oxidation on Hematite Photoanodes. *J. Am. Chem. Soc.* **2016**, 138, 2705–2711.
- 3. Nakamura, R.; Nakato, Y. Primary Intermediates of Oxygen Photoevolution Reaction on TiO<sub>2</sub> (Rutile) Particles, Revealed by in Situ FTIR Absorption and Photoluminescence Measurements. *J. Am. Chem. Soc.* **2004**, 126, 1290–1298.
- 4. Zhang, Y.; Zhang, H.; Liu, A.; Chen, C.; Song, W.; Zhao, J. Rate-Limiting O Id Formation Pathways for Water Oxidation on Hemitate. *J. Am. Chem. Soc.* **2018**, 140, 3264–3269.
- 5. Zhang, Y.; Zhang, Y.; Guo, W.; Johnston-Peck, A. C.; Hu, Y.; Song, X.; Wei, W Modulating multi-hole reaction pathways for photoelectrochemical water oxidation on gold nanocatalysts. *Energy Environ. Sci.* **2020**, 13, 1501–1508.
- 6. Kim, K.; Lee, S. H.; Choi, J. Y.; Shin, K. Fe<sup>3+</sup> to Fe<sup>2+</sup> conversion by plasmonically generated hot electrons from Ag nanoparticles: Surface-enhanced Raman scattering evidence. *J. Phys. Chem. C* **2014**, 118, 3359–3365.
- 7. Qi, Y.; Brasiliense, V.; Ueltschi, T. W.; Park, J. E.; Wasielewski, M. R.; Schatz, G. C.; Van Duyne, R. P. Plasmon-Driven Chemistry in Ferri-/Ferrocyanide Gold Nanoparticle Oligomers: A SERS Study. *J. Am. Chem. Soc.* **2020**, 142, 13120–13129.
- 8. Kim, Y.; Dumett Torres, D.; Jain, P. K. Activation Energies of Plasmonic Catalysts. *Nano Lett.* **2016**, 16, 3399–3407.
- 9. Kim, Y.; Smith, J. G.; Jain, P . Harvesting multiple electron-hole pairs generated through plasmonic excitation of Au nanoparticles. *Nat. Chem.* **2018**, 10, 763–769.

- 10. Bard, A . Inner-sphere heterogeneous electrode reactions. Electrocatalysis and photocatalysis: the challenge. *J. Am. Chem. Soc.* **2010**, 132, 7559–7567.
- 11. Eisenberg, M.; Silverman, H. P. Photo-Electrochemical Cells. *Electrochem. Acta* **1961**, 5, 1–12.
- 12. Haynes, W. M.CRC Handbook of Chemistry and Physics; CRC Press: 2008.
- 13. Villarreal, E.; Li, G. G.; Zhang, Q.; Fu, X.; Wang, H
  Effects on Ligand-Nanoparticle Interactions: A Plasmon-Enhanced Spectroscopic Study
  of Thiolated Ligand Adsorption, Desorption, and Exchange on Gold Nanoparticles. *Nano Lett.* **2017**, 17, 4443–4452.
- 14. Nakamura, I.; Negishi, N.; Kutsuna, S.; Ihara, T.; Sugihara, S.; Takeuchi, K oxygen vacancy in the plasma-treated TiO<sub>2</sub> photocatalyst with visible light activity for NO removal. *J. Mol. Catal. A Chem.* **2000**, 161, 205–212.
- 15. Sun, Y.; Egawa, T.; Shao, C.; Zhang, L.; Yao, X. EPR line broadening of F center in high-surface-area anatase titania nanoparticles prepared by MOCVD. *J. Cryst. Growth* **2004**, 268, 118–122.
- 16. Pan, X.; Yang, M. Q.; Fu, X.; Zhang, N.; Xu, Y . Defective TiO<sub>2</sub> with oxygen vacancies: Synthesis, properties and photocatalytic applicatio . *Nanoscale* **2013**, 5, 3601–3614.
- 17. Diebold, U. The surface science of titanium dioxide. Surf. Sci. Rep. 2003, 48, 53–229.
- 18. Priebe, J. B.; Radnik, J.; Lennox, A. J.; Pohl, M.; Karnahl, M.; Hollmann, D.; Grabow, K.; Bentrup, U.; Junge, H.; Beller, M.; Brückner, A. Solar Hydrogen Production by Plasmonic Au–TiO<sub>2</sub> Catalysts: Impact of Synthesis Protocol and TiO<sub>2</sub> Phase on Charge Transfer Efficiency and H<sub>2</sub> Evolution Rates. *ACS Catal.* **2015**, 5, 2137–2148.
- Priebe, J. B.; Karnahl, M.; Junge, H.; Beller, M.; Hollmann, D.; Brückner, A Reduction with Visible Light: Synergy between Optical Transitions and Electron Transfer in Au-TiO<sub>2</sub> Catalysts Visualized by in Situ Epr Spectroscopy. *Angew. Chem., Int. Ed.* 2013, 52, 11420–11424.
- 20. Hurum, D. C.; Agrios, A. G.; Gray, K. A.; Rajh, T.; Thurnauer, M. Explaining the Enhanced Photocatalytic Activity of Degussa P25 Mixed-Phase TiO<sub>2</sub> Using EPR. *J. Phys. Chem. B* **2003**, 107, 4545–4549.
- 21. C.; Wang, T. C.; Wong, M. S.; Gopal, N. Low temperature kinetics and energetics of the electron and hole traps in irradiated TiO<sub>2</sub> nanoparticles as revealed by EPR spectroscopy. *J. Phys. Chem. B* **2006**, 110, 11628–11634.